

Optical Structure and Proper-Motion Age of the Oxygen-rich Supernova Remnant 1E 0102–7219 in the Small Magellanic Cloud¹

Steven L. Finkelstein², Jon A. Morse², James C. Green³, Jeffrey L. Linsky³, J. Michael Shull³, Theodore P. Snow³, John T. Stocke³, Kenneth R. Brownsberger⁴, Dennis C. Ebbets⁴, Erik Wilkinson⁴, Sara R. Heap⁵, Claus Leitherer⁶, Blair D. Savage⁷, Oswald H. Siegmund⁸, & Alan Stern⁹

¹ *Based on observations with the NASA/ESA Hubble Space Telescope, obtained at the Space Telescope Science Institute, which is operated by the Association of Universities for Research in Astronomy, Inc. under NASA contract No. NAS5-26555.*

² *Department of Physics and Astronomy, Arizona State University, Tempe, AZ 85281*

³ *Center for Astrophysics and Space Astronomy, University of Colorado, Boulder, CO 80309*

⁴ *Ball Aerospace & Technologies Corp., Boulder, CO 80306*

⁵ *NASA/Goddard Space Flight Center, Greenbelt, MD 20771*

⁶ *Space Telescope Science Institute, Baltimore, MD 21218*

⁷ *Astronomy Department, University of Wisconsin, Madison, WI 53706*

⁸ *Space Sciences Laboratory, University of California - Berkeley, Berkeley, CA 94720*

⁹ *Southwest Research Institute, Boulder, CO 80302*

ABSTRACT

We present new optical emission-line images of the young supernova remnant (SNR) 1E 0102–7219 (hereafter E0102) in the Small Magellanic Cloud obtained with the *Hubble Space Telescope* (*HST*) Advanced Camera for Surveys (ACS). E0102 is a member of the oxygen-rich class of SNRs showing strong oxygen, neon, and other metal-line emissions in its optical and X-ray spectra, and an absence of hydrogen and helium. The progenitor of E0102 may have been a Wolf-Rayet star that underwent considerable mass loss prior to exploding as a Type Ib/c or IIL/b supernova. The ejecta in this SNR are generally fast-moving ($V > 1000 \text{ km s}^{-1}$) and emit as they are compressed and heated in the reverse shock. In 2003, we obtained optical [O III], H α , and continuum images with the ACS

Wide Field Camera. The [O III] image through the F475W filter captures the full velocity range of the ejecta, and shows considerable high-velocity emission projected in the middle of the SNR that was Doppler-shifted out of the narrow F502N bandpass of a previous Wide Field and Planetary Camera 2 image from 1995. Using these two epochs separated by ~ 8.5 years, we measure the transverse expansion of the ejecta around the outer rim in this SNR for the first time at visible wavelengths. From proper-motion measurements of 12 ejecta filaments, we estimate a mean expansion velocity for the bright ejecta of $\sim 2000 \text{ km s}^{-1}$ and an inferred kinematic age for the SNR of $\sim 2050 \pm 600$ years. The age we derive from *HST* data is about twice that inferred by Hughes et al. (2000, ApJ, 543, L61) from X-ray data, though our $1\text{-}\sigma$ error bars overlap. Our proper-motion age is consistent with an independent optical kinematic age derived by Eriksen et al. (2003, AIPC, 565, 419) using spatially resolved [O III] radial-velocity data. We derive an expansion center that lies very close to conspicuous X-ray and radio hotspots, which could indicate the presence of a compact remnant (neutron star or black hole).

Subject headings: ISM: supernova remnants: individual (1E 0102–7219) — stars: Wolf-Rayet

1. Introduction

Supernova remnants (SNRs) reveal how stars synthesize and distribute the elements heavier than H and He. Young SNRs with uncontaminated debris are among our best natural laboratories for understanding how nucleosynthesis operates in massive stars. Studying the SNR ejecta provides clues about the dynamics of supernova (SN) explosions, the composition and spectral type of progenitors, and ultimately about the chemical enrichment process in galaxies.

The oxygen-rich SNR 1E 0102–7219 (E0102) in the Small Magellanic Cloud (SMC) offers an exceptional opportunity for multi-wavelength, high resolution studies of a young SNR. E0102 is a vital object in the small class of oxygen-rich SNRs that contain filaments of uncontaminated debris from core-collapse supernovae. Out of the few (~ 10) known objects in the oxygen-rich class, E0102 is one of the most interesting because of its similarities to the prototype O-rich SNR, Cassiopeia A (Cas A) in the Galaxy. However, unlike Cas A, the sight-line to E0102 in the SMC has low interstellar extinction that allows us to gather data from the X-rays to the radio; yet it is close enough that we can still discern physically important scales.

E0102 was discovered by Seward & Mitchell (1981) in an *Einstein* X-ray observatory survey of the Magellanic Clouds. It is located in the SMC just northeast of the high-excitation H II region N76A (Henize 1956). Dopita, Tuohy, & Mathewson (1981) recognized E0102 as an O-rich SNR by virtue of its strong optical [O III] $\lambda\lambda$ 4959,5007 emission but complete lack of hydrogen emission from a network of filaments. Subsequent spectra by Tuohy & Dopita (1983) confirmed the presence of fast-moving, highly processed ejecta remarkable for showing emission from O and Ne only. They also estimated a kinematic age for the SNR of ~ 1000 years based on the velocity range they observed and its angular size.

E0102 exhibits the textbook forward/reverse shock structure that forms during the evolution of SNRs (Chevalier 1982). Emissions from the faint $\sim 44''$ diameter blast wave and bright $\sim 30''$ diameter shell of shocked ejecta have now been observed in exquisite detail across the electromagnetic spectrum from the ground and space (e.g., Amy & Ball 1993; Blair et al. 1989; Hayashi et al. 1994; Hughes et al. 2000; Gaetz et al. 2000; Stanimirović et al. 2005). The combined X-ray, UV, and optical emission spectra of the ejecta contains lines from O, Ne, C, Si, and Mg over a wide range of ionization states, from neutral to H-like species (Blair et al. 2000; Rasmussen et al. 2001). The comprehensive study by Flanagan et al. (2004) of the high-resolution *Chandra* X-ray spectrum shows that the highly ionized species are stratified; the higher ionization states occur at larger radii as the reverse shock propagates into the expanding ejecta. These authors also estimated a progenitor zero-age-main-sequence (ZAMS) mass of $\sim 32M_{\odot}$ based on their derived oxygen mass of $6M_{\odot}$ and heavy element abundance ratios, and comparing to theoretical predictions.

In this paper we present new optical images from the Advanced Camera for Surveys (ACS) aboard the *Hubble Space Telescope* (*HST*). We describe the observations in Sec. 2 and present the imaging results in Sec. 3. The new images capture the full velocity range of the emitting ejecta and reveal fresh details on the fastest filaments projected against the interior of the remnant. We compare our new [O III] image to one obtained previously with the Wide Field and Planetary Camera 2 (WFPC2) and measure proper motions of several outer filaments captured in both data sets. In Sec. 4 we discuss some implications of our proper-motion measurements and examine additional clues about the possible progenitor of E0102. Our conclusions are presented in Sec. 5. We assume a distance to the SMC of 59 kpc (e.g., van den Bergh 1999), where $0.1'' \approx 9 \times 10^{16}$ cm.

2. Observations

2.1. HST/ACS Wide Field Camera Images

We obtained images of E0102 with the ACS Wide Field Camera (WFC) aboard the *Hubble Space Telescope* in October 2003 (see Table 1) to select positions for future UV spectroscopic observations with the Cosmic Origins Spectrograph (COS; Green, Wilkinson & Morse 2003). Although a previous *HST* image through the F502N filter of WFPC2 exists (GO-6052, PI Morse; Blair et al. 2000), many of the brightest O-rich filaments through the interior of the SNR were Doppler-shifted out of the narrow bandpass. The new ACS WFC images were obtained using the Sloan g (F475W), i (F775W), and z (F850LP) broadband filters, the F550M (line-free continuum) filter, and the F658N ($H\alpha + [N II]\lambda\lambda 6548, 6583$) filter to capture the full velocity range of the emitting SNR ejecta, map the surrounding H II region emission, and characterize the stellar population along this line-of-sight through the Galaxy and SMC. We acquired the images through each filter using the standard line-dither observing pattern to fill in the inter-chip gap and identify hot pixels, while obtaining two exposures at each dither position to recognize cosmic rays. We used the IRAF/STSDAS¹⁰ environment for most of our image processing and analysis work. We began with the standard ACS pipeline processed (bias-subtracted, flat-fielded, geometric distortion-corrected, drizzled) images for our analysis. The final drizzled images had an image scale of $0''.05 \text{ pixel}^{-1}$ and we measured a typical point-source FWHM of 2.2 pixels in the visible passband filters, corresponding to a spatial resolution of $0''.11 \approx 1 \times 10^{17} \text{ cm}$.

Figure 1 shows a labeled ground-based ESO/MAMA U -band image of N76A and vicinity. The U -band image includes $[O II]\lambda\lambda 3727$ emission from the N76A nebula and E0102 SNR. In Figure 1 we have drawn the footprint of the ACS WFC field displayed in Figures 2 and 3, centered about $0.5'$ southwest of E0102. Our primary tracer of SNR ejecta emission is $[O III]$. Referring to the E0102 optical spectra of Tuohy & Dopita (1983) or Blair et al. (2000), the ACS WFC F475W filter includes ejecta emission from only the $[O III]$ lines at $\lambda\lambda 4959, 5007$, and (weak) $\lambda 4363$. Figure 2 shows an ACS color composite of E0102 and surroundings with the F550M continuum in blue, F475W $[O III]$ in green, and F658N $H\alpha + [N II]$ in red. Grayscale images of the individual $[O III]$ and $H\alpha + [N II]$ images are shown in separate panels of Figure 3. Figure 4 offers a close-up view of the complex filamentary structure in E0102, this time with the F775W image instead of F658N in red; this image

¹⁰IRAF is distributed by the National Optical Astronomy Observatories (NOAO), which is operated by the Association of Universities for Research in Astronomy, Inc. (AURA) under cooperative agreement with the National Science Foundation. The Space Telescope Science Data Analysis System (STSDAS) is distributed by the Space Telescope Science Institute.

reveals significant emission toward the middle of the SNR seen for the first time at $\sim 0.1''$ spatial resolution. The bright [O III] filaments are detected $\sim 50 - 60\sigma$ above the sky noise, and the fainter structures are detected at the $\sim 5 - 8\sigma$ level.

2.2. Alignment with HST/WFPC2 and Chandra/ACIS Images

Figure 5 compares the previous F502N WFPC2 Planetary Camera image and the new F475W ACS WFC image, each using [O III] emission to trace the optical filaments. The WFPC2 data were obtained ~ 8.5 years prior to the ACS images. We subtracted the two images in the bottom panel to highlight two features: (1) high-velocity emission through the interior of the SNR that is now included in the ACS bandpass (displayed in white); and (2) black-and-white edges where we have for the first time detected proper motions of several [O III] filaments around the periphery of the SNR. We later use the proper motions to derive an expansion center and age for E0102.

To detect ejecta motions between the two epochs, the [O III] images had to be aligned to sub-pixel accuracy. Based on previous kinematic data (e.g., Tuohy & Dopita 1983; Eriksen et al. 2001) we expect transverse motions of only $\lesssim 0.1''$, given our ~ 8.5 -year time baseline and 59 kpc distance to the SMC. We registered the 2003 ACS image to the 1995 WFPC2 image using the IRAF tasks GEOMAP and GREGISTER in order to compensate for differences in the image scales, rotations, and geometric distortion corrections. We selected 40 stars in the WFPC2 image (Figure 5) to use as tie points for registering the ACS image. The stars were chosen to provide adequate astrometric information across the field of the SNR, as well as high enough signal-to-noise ratios for accurate centroiding in the narrowband F502N WFPC2 Planetary Camera image without saturating in the broadband F475W ACS WFC image. The registration stars are circled in the left panel of Figure 6. We used a cubic polynomial fit to transform and align the images. The fit had r.m.s. residuals of ~ 0.1 pixels, corresponding to ~ 5 mas. Over the 8.5-year time baseline, a displacement of 5 mas corresponds to a transverse velocity of ~ 165 km s $^{-1}$ at the distance of the SMC, which we regard as our internal systematic uncertainty due to alignment errors. Additional uncertainties arise during our proper-motion measurement process that we discuss in Sec. 3.3. The final image scale in the registered data is that for the WFPC2 Planetary Camera of $0.04555''/\text{pixel}$ (Holtzman et al. 1995).

We also aligned a *Chandra* ACIS-S calibration image (Hughes et al. 2000) with the *HST* images, the same *Chandra* image that Blair et al. (2000) used in their X-ray comparison. The *Chandra* image had a live-time exposure length of 11 ksec. Since there are no common tie points (i.e., stars) in the optical and X-ray images, we used the IRAF task WREGISTER

and the spacecraft pointing information in the image headers to align the images. The uncertainty in the image registration is probably $\lesssim 1''$ due to *HST* guide star catalog astrometry errors, *Chandra* aspect solution errors, etc. The ACIS-S image captures primarily soft X-ray emission in the 0.6 – 1.5 keV range that includes several O, Ne, and Mg emission lines (e.g., Gaetz et al. 2000; Hughes et al. 2000). While there are several correspondences with the optical emission, the X-ray emission is more complete around the periphery of the SNR, hence the *Chandra* image was helpful for providing initial estimates of the SNR expansion center. We discuss below some new correlations between the X-rays and the optical emission seen in the ACS image, building on previous analyses (e.g., Gaetz et al. 2000; Blair et al. 2000). The *Chandra* ACIS-S image, deconvolved with 5 iterations of the STSDAS task LUCY, is shown in the right panel of Figure 6. The deconvolved image highlights small-scale emission features, particularly the bright filament along the southeast limb, several spoke-like features through the middle of the SNR, and a barely resolved blob just below the SNR geometric center.

3. Results and Analysis

3.1. Image Analysis

In the initial E0102 SN explosion, a shock wave drove out from the surface of the star, with the ejecta following slower behind it, but still moving with $V > 1000 \text{ km s}^{-1}$. As this blast wave has swept up ambient gas, it has slowed down to velocities lower than the fastest ejecta. A reverse shock has thus formed that decelerates and excites the ejecta (Blondin 2001). As in Cas A, emission from ejecta that have passed through the reverse shock in E0102 dominates its appearance in optical and X-ray emission-line images.

The images we obtained with the ACS show much more emission than the previous WFPC2 data. Notwithstanding the larger field of view of the ACS WFC as compared with the WFPC2 Planetary Camera, the ACS filter bandpasses we employed are also wider than those used with WFPC2. Nebular imaging with wide bandpasses usually creates problems for understanding which emission lines dominate in a particular region, but for young, metal-rich SNRs that exhibit relatively sparse optical emission-line spectra the confusion is minimized (e.g., Fesen et al. 2001; Morse et al. 2004). Our F475W ACS WFC image contains both lines of the [O III] $\lambda\lambda 4959, 5007$ doublet¹¹ and easily covers the entire velocity range of $\sim 6500 \text{ km s}^{-1}$ (Tuohy & Dopita 1983). However, one complication of the improved sensitivity and

¹¹H β and higher H Balmer lines might normally be confused with [O III] in the F475W filter, but the absence of H α emission in E0102 means that H β is absent as well, as shown in the spectra of Tuohy & Dopita

velocity coverage is that many more foreground/background stars (and galaxies) appear in the ACS images, many of which needed to be removed for the proper-motion analysis.

Figure 2 enables us to see more of the environment surrounding E0102 at high spatial resolution than previously possible. The high-ionization H II region N76A located in the lower-right portion of the image is highly filamentary. It appears yellow-ish in the color composite as a blend of primarily He II λ 4686 and [O III] $\lambda\lambda$ 4959, 5007 in the green (F475W) image and H α + [N II] $\lambda\lambda$ 6548, 6583 in the red (F658N) image. The red edges of the filaments suggest that the nebula is ionization bounded. We discuss possible implications of the proximity of E0102 to N76A in Sec. 4.2. Previous authors, including Tuohy & Dopita (1983), have commented on the diffuse halo of ionized gas immediately surrounding the network of E0102 ejecta filaments. There is a $\sim 10''$ gap between the filaments and this partial halo seen mainly in [O III] and partly in H α (Figure 3). A faint X-ray plateau and radio emission fill this gap (e.g., Gaetz et al. 2000). The outer edge of the X-ray plateau has been interpreted as marking the propagation of the blast wave into the circumstellar medium and the radio emission is likely synchrotron emission from electrons accelerated in magnetic fields compressed behind the blast wave. Hughes et al. (2000) determined that the abundances from the X-ray blast wave plateau are consistent with shocked low-metallicity SMC interstellar gas. The optical spectrum of the surrounding diffuse halo (Tuohy & Dopita 1983) shows it to be stationary and highly ionized, with strong [O III] and He II emission, reminiscent of the extended narrow-line regions in active galactic nuclei (Morse et al. 1996a). Morse et al. (1996b) showed that a similar halo around the O-rich SNR N132D in the Large Magellanic Cloud is likely ionized by high-energy photons produced by shocks within the SNR itself, and we favor this scenario in E0102 as well. The H α + [NII] image in the bottom panel of Figure 3 shows some clumpiness in the external medium, including a series of small cloudlets just to the north of E0102. These may be part of an extended plume from N76A, or they may be wind material from the progenitor of E0102.

The close-up color composite image in Figure 4 identifies the O-rich ejecta in green. The ejecta are composed of long sinuous filaments with distortions and protrusions reminiscent of Rayleigh-Taylor instabilities and individual knots down to the resolution limit of our images. Overall the detailed structure of E0102 closely resembles the optical filaments in Cas A (e.g., Fesen et al. 2001), though E0102 is several times larger in size. The optical emission is obviously asymmetrical; the entire eastern edge is almost continuous, but the western and northern portions show much less emission. There is even a broken region in the southwest that resembles the break-out of the northeastern jet in Cas A. The difference image in

(1983) and Blair et al. (2000).

Figure 5 highlights in white the regions where we detected emission with ACS F475W that was Doppler-shifted out of the WFPC2 F502N bandpass. The WFPC2 F502N filter has a FWHM width of about $\pm 900 \text{ km s}^{-1}$; debris moving faster than this was therefore missed in the WFPC2 image. The most stunning example is the bright backward S-shaped emission structure that starts in the south-southwest, extends through the middle of the SNR, and bends towards the northeast. In fact this is the brightest optical emission in E0102. The kinematic data of Tuohy & Dopita (1983) and Eriksen et al. (2001) show that most of the gas from this bright structure moves at about -1000 km s^{-1} at the south and north edges and up to -2100 km s^{-1} through the middle — i.e., it is associated with the approaching side of the ejecta shell. There is also bright emission from the western limb now seen in the ACS image that likewise shows velocities of about -1000 km s^{-1} .

3.2. Comparison with the X-rays

The new ACS images afford us the chance to compare the optical emission distribution with the X-ray emitting gas. The left image in Figure 7 shows a color composite of the 1999 *Chandra* ACIS-S image with the ACS [O III] F475W and red continuum F775W images of E0102. The correspondences between the X-rays and optical emission along the outer rim of E0102 have been discussed previously by Gaetz et al. (2000) and Blair et al. (2000). Here we are able to add new information about the emission through the interior of the SNR. The right panel of Figure 7 shows three color-coded contours of the X-ray emission overlaid on the ACS F475W [O III] image. With the full range of [O III] emission now available, there are several new interesting correlations with the X-rays. The bright southern portion of the backward S-shaped [O III] complex coincides with the brightest X-ray spoke from the southwest portion of the outer ring towards the middle of the SNR, connecting to the central blob. The correspondence is not exact; the spoke extends from the ring to the center in both wavelength regimes, but in the optical the emission widens as it reaches the center. At the point where it starts to widen, the X-ray spoke shows a bulge or knot but then narrows to its previous thickness. About $10''$ to the east of this spoke there is considerable optical emission with no X-ray counterparts. The northern section of the backward S-shaped [O III] complex likewise shows only faint X-ray emission associated with it. However the other obvious X-ray spoke winding from the western edge of the ring towards the middle hotspot lies adjacent to a similar optical spoke. The X-ray spoke connects to the central region in a small loop. Around the inner boundary of this loop lies a similar but smaller optical loop of emission. The two spokes with optical and X-ray emission that extend from the outer ring of emission to the central hotspot surround an emission void perhaps best seen in the side-by-side images of Figure 6. (The bright star in the optical image that projects near the

middle of this emission void is probably not physically associated with the SNR.)

In summary, there are several regions through the interior of the remnant where we see both X-ray and optical emission, but on close scrutiny the two emissions tend to lie adjacent to each other rather than exactly coinciding. This spatial arrangement between the optical and X-ray emission can be understood if it represents gradients in ejecta densities in the shocked gas. We note that this relationship demonstrates the need for data from complementary wavelength regimes in order to gain a full picture of the SNR. Similar results are seen in Cas A (e.g., DeLaney et al. 2004; Fesen et al. 2005). We also stress that the brightest [O III] emission projects across the middle of the SNR, not around the edges. The optical emission distribution implies that the ejecta are not confined solely to a ring geometry as modeled by Flanagan et al. (2004) for the X-ray emitting ejecta. A thick X-ray ring may still hold much of the ejecta mass but the overall geometry of the SNR is likely more complicated. In Cas A, for example, the optical emission generally lies in ring-like structures situated on the surface of an expanding shell (Lawrence et al. 1995). Such could be the case with much of the optical emission in E0102.

3.3. Proper-Motion Measurements

We used the 1995 epoch and 2003 epoch *HST* [O III] images to measure proper motions of fast-moving ejecta knots and filaments around the periphery of E0102. Ejecta found at the largest projected radii move roughly transverse to our line of sight and the emission is therefore captured in both the previous narrowband F502N WFPC2 and the new broadband F475W ACS WFC images. The difference image in Figure 5 shows that the same features are seen at both epochs in many locations around the SNR and that the features have moved outward between 1995 and 2003. Measuring the transverse velocities of fast-moving optical ejecta has long been one of our most important tools for understanding the dynamics (e.g., expansion center and age) of Cas A (Minkowski 1968; van den Bergh 1971; Thorstensen et al. 2001; Morse et al. 2004; Fesen et al. 2005). The exquisite spatial resolution of *HST* allows us to make such measurements for the first time in E0102 at the 59 kpc distance of the SMC. The E0102 progenitor is thought to have had a ZAMS mass of at least 25–32 M_{\odot} (Blair et al. 2000; Flanagan et al. 2004) and the proper-motion measurements may bear on the location of a compact remnant such as a neutron star or black hole. After presenting our proper-motion measurements, we return to the topic of the progenitor star and its location in Sec. 4.

We measured transverse velocities of a number of optical knots and filaments in E0102 using a software package developed by P. Hartigan, S. Heathcote, and one of us (JAM)

that is optimized to detect motions of extended nebular objects. The software performs a subtraction-based cross-correlation following an algorithm described by Currie et al. (1996). It has been used to measure proper motions of shock structures and outflows in multi-epoch *HST* images of the η Carinae system and several Herbig-Haro jets (Morse et al. 2001; Hartigan et al. 2001, 2005; Reipurth et al. 2002; Bally et al. 2002). A small rectangular image region from one epoch is compared to a larger region on the second epoch image, and the pixel-by-pixel difference squared is calculated and summed over the region covered by the smaller image. The sum of the squares of the differences is stored in a correlation image for each position as the first epoch feature is raster scanned across a section of the second epoch image. The difference squared is a minimum where the feature in the two epochs best aligns. After the raster scan, we invert the correlation image so that the difference-squared minimum is a maximum. In general, the correlation peaks (inverted minima) resembled stellar images. We use a modified form of the flux-weighted centroiding algorithm and uncertainty estimate in the APPHOT package of IRAF to calculate the peak position to within a fraction of a pixel. The code computes the mean and mean error of the x and y marginal distributions using points within the specified centering box. The pixel shift of the peak from the center of the correlation image then indicates both the magnitude and direction of the proper motion of the feature of interest between the two epochs. In addition to the centroiding uncertainties, there are also systematic uncertainties due to the accuracy of the image registration and possible photometric variations of the measured filaments. We noted the magnitude of the former in Sec. 2.2; the latter could arise either from bandpass differences of the two *HST* cameras used, rapid radiative cooling and evolution of the emitting filaments, or a combination of both. Finally, by defining a “source” position (in this case the expansion center of the SNR), along with the distance to the target (59 kpc) and the time interval between observations (~ 8.5 years), the software calculates the kinematic age of each feature assuming no deceleration of the ejecta.

Regions used for measuring proper motions were selected by blinking the registered [O III] images on the computer screen. The difference image in Figure 5 provides a guide to those features around the periphery of the SNR where features appear in both epochs and outward motions are observed. We defined individual regions around filaments and knots that were large enough to generate clean cross-correlation peaks but small enough to minimize differential motions within the region due to the curvature of the outer rim of the SNR. Background stars were located in close proximity to some of the selected ejecta filaments and had to be removed. If stars are included in the measurement, they can skew the results because the stars do not move in the registered images while the filaments do, producing multiple correlation peaks. We eliminated the stars by subtracting registered, line-free continuum images from the [O III] images, leaving only the emitting filaments and knots.

For the WFPC2 data, we scaled and subtracted an F547M image; for the ACS WFC data, we scaled and subtracted the F550M image. We avoided a few regions where subtracting bright stars projected on or near filaments left noticeable residual flux. Ultimately we selected 12 regions, mostly around the eastern rim of the SNR, for measuring proper motions. These regions are identified on the continuum-subtracted ACS WFC [O III] image in Figure 8.

Table 2 lists the results for our proper-motion measurements for the 12 regions we selected, where each region is labeled in Figure 8. The table includes the region number; X and Y pixel location in the registered images of each region center; the tangential velocity and derived uncertainty from the centroiding procedure; the uncertainty as a fraction of the measured velocity; the position angle of the region center relative to the chosen expansion center (PA-Center), the position angle of the direction of motion (PA-Motion), and the difference between these two angles (Δ PA); and the inferred kinematic age. The bottom row shows average values of some of the measured quantities. In particular, we measured tangential velocities ranging from $\sim 1350 - 2940 \text{ km s}^{-1}$, and an average expansion of $1966 \pm 193 \text{ km s}^{-1}$. This average expansion velocity corresponds to an offset of $0.060'' \pm 0.006''$, or slightly over one pixel, during the 8.5 year time baseline. The uncertainties listed in Table 2 reflect the quality of the correlation measurements, and are approximately commensurate with the r.m.s. uncertainty in the image alignment. We must also recognize that photometric changes can occur in the rapidly cooling, metal-rich optical filaments as the reverse shock propagates through the ejecta (e.g., see the discussion in Morse et al. 2004) that could affect the proper-motion measurements, though similar debris in Cas A tend to remain visible for several decades (Thorstensen et al. 2001).

Calculating the kinematic age requires that we supply an estimate of the expansion center, i.e., where the explosion occurred. Table 2 assumes this to be the geometric center of the SNR, estimated from the ring of reverse shock emission in the *Chandra* X-ray image. Using the IRAF routine RINGPARS in the CTIO FABRY package, intensity peaks in horizontal and vertical cross-cuts were measured using Gaussian fits and the (X,Y) center of the X-ray ring was calculated. The geometric center is located at a position of RA $01^{\text{h}}04^{\text{m}}02^{\text{s}}.08$, DEC $-72^{\circ}01'52''.5$ (J2000). Using this center, as marked on Figure 8 with a '+', the average inferred kinematic age is ~ 2123 years.

Alternatively, we empirically determined the expansion center by assuming that the transverse motions of the ejecta are radially outward. Figure 8 shows the directions of the proper motions for all the regions we measured. Assuming radial motions, these arrows should, in principle, intersect at the position of the explosion. Even with the uncertainties in the individual measurements, it is apparent when looking at Figure 8 that the arrows on average trace back to a position south of the X-ray geometric center. Using vector addition

— i.e., forcing the average ΔPA to be zero degrees — we derive a proper-motion center at RA $01^h04^m02^s.05$, DEC $-72^\circ01'54''.9$ (J2000). Using this expansion center position, Table 3 lists the new position angles for each region and a revised average kinematic age of 2054 ± 584 years.¹² The 1σ uncertainty in the average ΔPA is ± 14.8 degrees. Projecting this back to the derived expansion center position, we define a 1σ error circle of radius $3.4''$. Our derived expansion center (marked by an ‘X’) and 1σ error circle are drawn in Figure 8. The geometric center of the X-ray ring is located slightly east and $\sim 2.4''$ to the north ($\sim 0.7\sigma$ in projection) of the derived expansion center.

4. Discussion

4.1. Geometry, Expansion Center, and Kinematic Age

The ability to see the full velocity range of optical [O III] emission in E0102 (Figure 3) adds to our understanding of the geometry and dynamics of this SNR. Because much of the emission from the central region seen in the ACS data was Doppler-shifted out of the narrow bandpass of the WFPC2 data, we conclude that these high-velocity ejecta must lie on the front or rear side of an expanding shell. The [O III] Fabry-Perot data cube of Eriksen et al. (2001) shows that most of this emission is blueshifted up to $\sim -2100 \text{ km s}^{-1}$. Neither this highly blueshifted emission nor several other filaments through the middle of the SNR have X-ray kinematic counterparts while in many other parts around the outer rim the association seems clear. The optical emission distribution requires that a shell-like component be included in models of E0102, even if most of the mass traced in X-rays is confined to a ring-like structure (Flanagan et al. 2004). For completeness we note that, to our eyes, the main ring of (reverse shock) X-ray emission in the *Chandra* images shown in Gaetz et al. (2000), Flanagan et al. (2004), and our Figures 6 and 7 is clearly not circular, as has usually been assumed in previous models, but is somewhat elliptical with the major axis aligned along $\text{PA} \sim -15^\circ$.

Our proper-motion results provide vital missing pieces to the E0102 puzzle and allow us to pull together a number of loose threads. Our derived expansion center projects in the middle of the backward S-shaped filament complex we described above and aligns with the break in the optical rim in the southwest that is reminiscent of the Cas A northeastern jet. Eriksen et al. (2001) noted peculiar [O III] kinematics in the central region of their Fabry-

¹²Throwing out the highest and lowest inferred ages yields the same average age and a reduced uncertainty of 2053 ± 450 years. Throwing out the two highest and two lowest values also yields a similar age and further reduced uncertainty of 2033 ± 320 years.

Perot data cube, i.e., low-velocity emission projected against the fast-moving approaching debris (see also the discussion in Flanagan et al. 2004). Moreover, our result places the expansion center at or near to the X-ray hotspot in the SNR middle to which all the X-ray spokes attach (Gaetz et al. 2000; Flanagan et al. 2004). It also coincides with the central radio emission blob that Amy & Ball (1993) suspected may be the site of a plerion. In fact, a bar of radio emission, surrounded by X-ray emission, runs northeast-southwest along PA $\sim 50^\circ$ directly through our expansion center. It is possible that this structure could be jet-induced, similar to Cas A (Hwang et al. 2004), and that both the radio and X-ray blobs trace emission associated with a compact object, perhaps a neutron star or black hole.

Our proper-motion age for E0102 of 2054 ± 584 years agrees well with the expansion age of ~ 2100 years estimated by Eriksen et al. (2001) based on their fitting an expansion ellipse to Fabry-Perot [O III] radial-velocity data, but is only marginally consistent with the X-ray expansion age of ~ 1000 years estimated by Hughes et al. (2000). We place the site of the explosion squarely at the X-ray/radio blob of interest just south of the geometric center. The asymmetric distribution of optical ejecta and the slightly oval-shaped morphology in the X-rays could be due to an asymmetric explosion or possibly a density gradient in the circumstellar medium (mass loss from the progenitor star). For the latter case, we would infer higher circumstellar densities in the south, east, and near side, and lower densities in the north, west, and far side. Using the *Chandra* image, we measure a blast wave expansion radius from our derived expansion center of 7.2 pc ($\sim 25.2''$) towards the north roughly at PA $\sim -15^\circ$ and 5.6 pc ($\sim 19.5''$) towards the south at PA $\sim 165^\circ$. The expansion has proceeded $\sim 28\%$ farther to the north than to the south. Adopting an expansion age of 2100 years, the blast wave has propagated to the north with a mean velocity of ~ 3360 km s $^{-1}$ and to the south with a mean velocity of ~ 2610 km s $^{-1}$. Probably the blast wave began expanding at a speed of $\gtrsim 10,000$ km s $^{-1}$ and has now slowed (as circumstellar material is swept up) to a value somewhat below the implied mean velocity in a particular direction. We predict not only a north-south asymmetry in a future X-ray measurement of the blast wave expansion, but also higher reverse shock velocities and lower densities in the north, consistent with the lack of optical emission. Higher X-ray temperatures to the north and higher densities to the south are precisely what Sasaki et al. (2005) infer in a new analysis of a combined far-UV and X-ray data set on E0102. Because of the noted asymmetries, we urge caution in using global average values to describe the geometry, dynamics, and evolution of E0102 when comparing its parameters to model predictions (e.g., Chevalier 2005); both the X-ray and optical data imply directional variations.

4.2. Clues to the E0102 Progenitor: Spying on the Neighbors

The E0102 progenitor may have been a very massive main-sequence star that underwent substantial mass loss during its late stages of evolution. The resulting SN explosion was likely of Type IIL/b or Ib/c (Blair et al. 2000; Chevalier 2005), depending on whether a thin H envelope was present when the explosion occurred (to date there is no indication of fast-moving H or He debris mixed in with the expanding ejecta). The fast-moving O-rich ejecta we observe are broadly consistent with the predictions of models of nucleosynthesis within the helium-burnt layers of evolved massive stars (Woosley et al. 1993; Thielemann et al. 1996; Nomoto et al. 1997), though in detail comparing to any particular set of models is complicated by an object’s specific initial conditions (i.e., metallicity, ZAMS mass, binarity) and by the fact that only some of the ejecta are emitting and can be analyzed.

Blair et al. (2000) compared their relative elemental abundance estimates to the nucleosynthesis predictions of Nomoto et al. (1997) and found the best agreement with models that had progenitor ZAMS masses $> 25M_{\odot}$. Flanagan et al. (2004) obtained similar relative abundance ratios from the *Chandra* data, especially for O/Ne, but also estimated a total oxygen mass in the ejecta of $\sim 6 M_{\odot}$. Again comparing to the Nomoto et al. models, they inferred a progenitor ZAMS mass of $\sim 32 M_{\odot}$. Both Blair et al. and Flanagan et al. noted that the models under-predict the amount of Ne by a factor of ~ 2 . The models also predict that O-burning products such as S, Ca, and Ar should be observed, but in fact they are not, leading us to question the true relevance of these models for making detailed comparisons.

In order to guide theoretical efforts to model the progenitor and SN type of E0102, we suggest that meaningful constraints can be gleaned by examining the local stellar population with which E0102 is associated. Such constraints will be independent of the ejecta abundances and masses — as well as their assumptions about geometries, ionization states, filling factors, etc. — inferred from observations of E0102 itself. For example, one of the reasons for believing that η Carinae is an evolved supermassive star is that there are main-sequence O3 stars in close proximity (e.g., Walborn 1995). One needs to be wary of issues such as actual physical co-location and coeval formation, but for E0102 there appears to be a relevant connection.

Figure 1 shows the N76A nebula that surrounds the OB association Hodge 53 (cf., Massey et al. 2000). E0102 lies a projected distance of only ~ 10 pc to the northeast of the nebula edge. N76A’s high ionization requires a high effective temperature for the main exciting source SMC WR7 (= AzV 336a; Pakull & Bianchi 1991). Moreover the round appearance of N76A is more consistent with a Wolf-Rayet bubble than a star-forming H II region like the Orion nebula. Niemela et al. (2002) found that SMC WR7 is a double-lined WN2 + O6 spectroscopic binary with a period of 19.56 d. These authors constrain the

minimum masses to be ~ 18 and $34 M_{\odot}$ for the WN2 and O6 components, respectively. In addition, although coeval formation is questionable, Massey et al. (2000) suggest that the ZAMS mass of the WN2 progenitor star in the SMC WR7 system is $> 50 M_{\odot}$ based upon the turn-off mass of the cluster. We speculate that a plausible progenitor candidate for E0102 is a star with properties similar to the WN2 component of SMC WR7 (Massey & Duffy 2001), given the similar strong He II $\lambda 4686$ emission of the E0102 halo and the general agreement of the fast-moving ejecta abundances with models of Wolf-Rayet atmospheres (e.g., Woosley et al. 1993). For such a progenitor star, the SN explosion was likely of Type Ib/c.

5. Conclusion

A new imaging data set from the *Hubble Space Telescope* Advanced Camera for Surveys reveals spectacular details in the O-rich SNR 1E 0102–7219 in the SMC. We used the broadband SDSS g (F475W) filter to capture the full [O III] $\lambda\lambda 4959, 5007$ velocity range of the ejecta. Many high-velocity knots and filaments projected through the middle of the SNR are seen for the first time at $\sim 0.1''$ resolution. We discuss their morphology, kinematics, and relationship to soft X-ray emission observed in a *Chandra* ACIS-S image. The wide field of view of the ACS images also allows us to examine the circumstellar environment of E0102. A narrowband H α + [N II] (F658N) image shows considerable inhomogeneity in the surrounding medium and a possible physical association between some of the gas in the halo of E0102 and the nearby N76A nebula.

We compared the 2003 ACS [O III] image to a 1995 narrowband WFPC2 Planetary Camera [O III] image and measured tangential expansion velocities in 12 regions around the periphery of the SNR. We find a mean expansion velocity for the optical ejecta of ~ 2000 km s $^{-1}$ and a kinematic age for E0102 of $\sim 2050 \pm 580$ years. Our kinematic age agrees with a recent estimate of Eriksen et al. (2001) based on spatially resolved [O III] radial-velocity data, but is a factor of two longer than found by Hughes et al. (2000) using multi-epoch, low-resolution X-ray images (although it is within 2σ).

The ejecta proper motions we measured trace back to an expansion center $\sim 2.4''$ south of the geometric center of the *Chandra* X-ray image. The 1σ error circle of our expansion center encompasses the conspicuous radio and X-ray blobs noted in previous studies (e.g., Amy & Ball 1993; Gaetz et al. 2000; Flanagan et al. 2004). Our kinematic data provide additional evidence for believing that a compact remnant (neutron star or black hole) may be associated with the central hotspot emissions. E0102’s proximity to the N76A Wolf-Rayet nebula and Hodge 53 OB association leads us to speculate that the E0102 progenitor may have been a very massive ($> 50 M_{\odot}$) main-sequence star that underwent considerable mass

loss as it evolved through a WN phase before exploding as a Type Ib/c supernova.

We thank the referee for carefully reviewing the manuscript and recommending changes that significantly improved the fidelity of the results. This work has been supported by NASA grant NAG5-12279 to the University of Colorado and the COS Science Team.

REFERENCES

- Amy, S.W., & Ball, L. 1993, *ApJ*, 411, 761
- Bally, J., Heathcote, S., Reipurth, B., Morse, J., Hartigan, P., & Schwartz, R. 2002, *AJ*, 123, 2627
- Blair, W.P., Raymond, J.C., Danziger, J., & Matteucci, F. 1989, *ApJ*, 338, 812
- Blair, W.P., Morse, J.A., Raymond, J.C., Kirshner, R.P., Hughes, J.P., Dopita, M.A., Sutherland, R.S., Long, K.S., & Winkler, P.F. 2000, *ApJ*, 537, 667
- Blondin, J.M. 2001, in *Young Supernova Remnants*, eds. S.S. Holt & U. Hwang (AIP: New York), 59
- Chevalier, R.A. 1982, *ApJ*, 258, 790
- Chevalier, R.A. 2005, *ApJ*, 619, 839
- Currie, D.G., Dowling, D.M., Shaya, E.J., Hester, J., Scowen, P., Groth, E.J., Lynds, R., O’Neil, E.J. Jr., & the Wide Field/Planetary Camera Instrument Definition Team 1996, *AJ*, 112, 1115
- Delaney, T., Rudnick, L., Fesen, R.A., Jones, T.W., Petre, R., & Morse, J.A. 2004, *ApJ*, 613, 343
- Dopita, M.A., Tuohy, I.R., & Mathewson, D.S. 1981, *ApJ*, 248, L105
- Eriksen, K.A., Morse, J.A., Kirshner, R.P., & Winkler, P.F. 2001, in *Young Supernova Remnants*, eds. S.S. Holt & U. Hwang (AIP: New York), 193
- Fesen, R.A., Hammel, M.C., Morse, J.A., Chevalier, R.A., Borkowski, K.J., Dopita, M.A., Gerardy, C.L., Lawrence, S.S., Raymond, J.C., & van den Bergh, S. 2005, *ApJ*, submitted
- Fesen, R.A., Morse, J.A., Chevalier, R.A., Borkowski, K.J., Gerardy, C.L., Lawrence, S.S., & van den Bergh, S. 2001, *AJ*, 122, 2644

- Flanagan, K.A., Canizares, C.R., Dewey, D., Houck, J.C., Fredericks, A.C., Schattenburg, M.L., Markert, T.H., & Davis, D.S. 2004, *ApJ*, 605, 230
- Gaetz, T.J., Butt, Y.M., Edgar, R.J., Eriksen, K.A., Plucinsky, P.P., Schlegel, E.M., & Smith, R.K. 2000, *ApJ*, 534, L47
- Green, J.C., Wilkinson, E., & Morse, J.A. 2003, *SPIE*, S164, 17
- Hartigan, P., Heathcote, S., Morse, J., Reipurth, B., and Bally, J. 2005, *AJ*, in press
- Hartigan, P., Morse, J., Reipurth, B., Heathcote, S., & Bally, J. 2001, *ApJ*, 559, L157
- Hayashi, I., Koyama, K., Ozaki, M., Miyata, E., Tsunemi, H., Hughes, J.P., & Petre, R. 1994, *PASJ*, 46, L121
- Henize, K.G. 1956, *ApJS*, 2, 315
- Holtzman, J., et al. 1995, *PASP*, 107, 156
- Hughes, J.P., Rakowski, C.E., & Decourchelle, A. 2000, *ApJ*, 543, L61
- Hwang, U., et al. 2004, *ApJ*, 615, L117
- Lawrence, S.S., MacAlpine, G.M., Uomoto, A., Woodgate, B.E., Brown, L.W., Oliverson, R.J., Lowenthal, J.D., & Liu, C. 1995, *AJ*, 109, 2635
- Massey, P., & Duffy, A.S. 2001, *ApJ*, 550, 713
- Massey, P., Waterhouse, E., DeGioia-Eastwood, K. 2000, *AJ*, 117, 2217
- Minkowski, R. 1968, in “Stars and Stellar Systems”, 7, 623
- Morse, J.A., Blair, W.P., Dopita, M.A., Hughes, J.P., Kirshner, R.P., Long, K.S., Raymond, J.C., Sutherland, R.S., & Winkler, P.F. 1996b, *AJ*, 112, 509
- Morse, J.A., Fesen, R.A., Chevalier, R.A., Borkowski, K.J., Gerardy, C.L., Lawrence, S.S., & van den Bergh, S. 2004, *ApJ*, 614, 727
- Morse, J.A., Kellogg, J.R., Bally, J., Davidson, K., Balick, B., & Ebbets, D. 2001, *ApJ*, 548, 207
- Morse, J.A., Raymond, J.C., & Wilson, A.S. 1996a, *PASP*, 108, 426
- Niemela, V.S., Massey, P., Testor, G., & Giménez Benítez, S. 2002, *MNRAS*, 333, 347

- Nomoto, K., Hashimoto, M., Tsujimoto, T., Thielemann, F.-K., Kishimoto, N., Kubo, Y., & Nakasoto, N. 1997, *Nuc. Physics*, A616, 79c
- Pakull, M., & Bianchi, L. 1991, in *Proc. IAU Symp. 143, Wolf-Rayet Stars and Interrelations with Other Massive Stars in Galaxies*, eds. K.A. van der Hucht & B. Hidayat (Kluwer: Dordrecht), p. 425
- Rasmussen, A.P., Behar, E., Kahn, S.M., den Herder, J.W., & van der Heyden, K. 2001, *A&A*, 365, L231
- Reipurth, B., Heathcote, S., Morse, J., Hartigan, P., & Bally, J. 2002, *AJ*, 123, 362
- Sasaki, M., Gaetz, T.J., Blair, W.P., Edgar, R.J., Morse, J.A., & Plucinsky, P.P. 2005, *ApJ*, submitted
- Seward, F.D., & Mitchell, M. 1981, *ApJ*, 243, 736
- Stanimirović, S., Bolatto, A.D., Sandstrom, K., Leroy, A.K., Simon, J.D., Gaensler, B.M., Shah, R.Y., & Jackson, J.M. 2005, *ApJ*, in press
- Thielemann, F.-K., Nomoto, K., & Hashimoto, M.-A. 1996, *ApJ*, 460, 408
- Thorstensen, J.R., Fesen, R.A., & van den Bergh, S. 2001, *AJ*, 122, 297
- Tuohy, I.R., & Dopita, M.A. 1983, *ApJ*, 268, L11
- Tuohy, I.R., Dopita, M.A., & Mathewson, D.S. 1981, *ApJ*, 248, L105
- van den Bergh, S. 1971, *ApJ*, 165, 457
- van den Bergh, S. 1999, in *New Views of the Magellanic Clouds*, IAU Symposium No. 190, eds. Y.-H. Chu, N. Suntzeff, J. Hesser, & D. Bohlender, p. 569
- Walborn, N.R. 1995, *RMxAC*, 2, 51
- Woosley, S. E., Langer, N., & Weaver, T. A. 1993, *ApJ*, 411, 823

Table 1. ACS Observations of 1E0102-9217

Data Set	Exposure Time (sec)	Date	Central Wavelength (Å)	$\Delta\lambda$ (Å)	Filter
J8R802010	760	15 Oct 2003	4760	1458	F475W
J8R802020	900	15 Oct 2003	5580	547	F550M
J8R802030	720	15 Oct 2003	6584	78	F658N
J8R802040	720	15 Oct 2003	9445*	1229	F850LP
J8R802050	720	15 Oct 2003	7764	1528	F775W

Note. — * The 850LP profile is asymmetrical, with the peak throughput at $\sim 9000\text{\AA}$.

Table 2. Proper Motions of 1E 0102-7219 and Ages Derived from X-ray Geometric Center

Region	x (pixels)	y (pixels)	Velocity (km/s)	V error (km/s)	Verr/V	PA-Center (Deg from N)	PA-Motion (Deg from N)	Δ PA (Deg from N)	Inferred Age (Years)
1	817.0	1230.0	1746.8	128.4	0.07	47.5	49.0	-1.5	1840.4
2	733.0	1178.0	2483.6	285.4	0.12	66.4	63.9	2.5	1514.1
3	698.0	1041.0	2074.5	165.5	0.08	93.6	116.4	-22.8	1880.8
4	727.0	967.0	2588.5	284.1	0.11	108.7	94.5	14.2	1437.0
5	748.0	910.0	1690.7	184.5	0.11	120.6	95.0	25.6	2235.8
6	715.0	870.0	1356.2	135.0	0.10	123.5	120.0	3.5	3251.7
7	793.0	857.0	2009.5	138.2	0.07	134.2	116.6	17.6	1858.2
8	844.0	790.0	1392.2	80.0	0.06	149.7	141.5	8.2	2879.7
9	1096.0	688.0	1737.4	78.1	0.05	194.1	181.6	12.5	2828.5
10	1284.0	911.0	2013.0	132.5	0.07	242.1	227.7	14.4	2027.6
11	1250.0	970.0	2940.0	587.7	0.20	250.0	272.0	-22.0	1148.1
12	1226.0	1279.0	1556.9	114.2	0.07	314.3	325.7	-11.4	2572.1
Average			1965.8	192.8	0.09			3.4 ± 15.4	2122.8 ± 644.4

Note. — The first three columns give the number of each of the twelve regions, and the pixel coordinates of those regions on the registered images. Column four gives the tangential velocity of each region, which was computed using our proper motion code. The next column estimates the uncertainty in that velocity, as calculated by the centroiding algorithm in our proper motion code. The seventh and eight columns list two position angles (PAs), where PA-Center is the angle from North each filament is moving with respect to the geometric center, and PA-Motion is the angle from North each filament is moving with respect to its current position. Δ PA is the difference in these two angles. The last column gives the inferred kinematic age, based on the velocity given by the proper motions, the distance to the SMC, and the time between epochs. The geometric center, based on the X-ray emission, was assumed to be at pixel (1002,1060), corresponding to RA $01^h04^m02^s.08$, DEC $-72^\circ01'52''.5$ (J2000).

Table 3. Ages Derived from Proper-Motion Derived Center

Region	PA-Center (Deg from N)	PA-Motion (Deg from N)	Δ PA (Deg from N)	Inferred Age (Years)
1	40.4	49.0	-8.6	2138.5
2	58.0	63.9	-5.9	1658.5
3	83.8	116.4	-32.6	1911.4
4	98.3	94.5	3.8	1394.1
5	110.7	95.0	15.7	2088.2
6	115.3	120.0	-4.7	3037.8
7	125.3	116.6	8.7	1661.5
8	143.3	141.5	1.8	2494.0
9	195.7	181.6	14.1	2446.0
10	250.8	227.7	23.1	1871.2
11	261.2	272.0	-10.8	1074.8
12	321.0	325.7	-4.7	2872.1
Average			0.0 ± 14.8	2054.0 ± 584.0

Note. — Expansion velocities and ages based on minimizing the value of Δ PA. Columns two and three list the modified PAs that were measured from minimizing Δ PA. Column four lists the Δ PAs, and the last column lists the inferred kinematic age. The proper-motion derived center lies at RA $01^h04^m02^s.05$, DEC $-72^\circ01'54''.9$ (J2000).

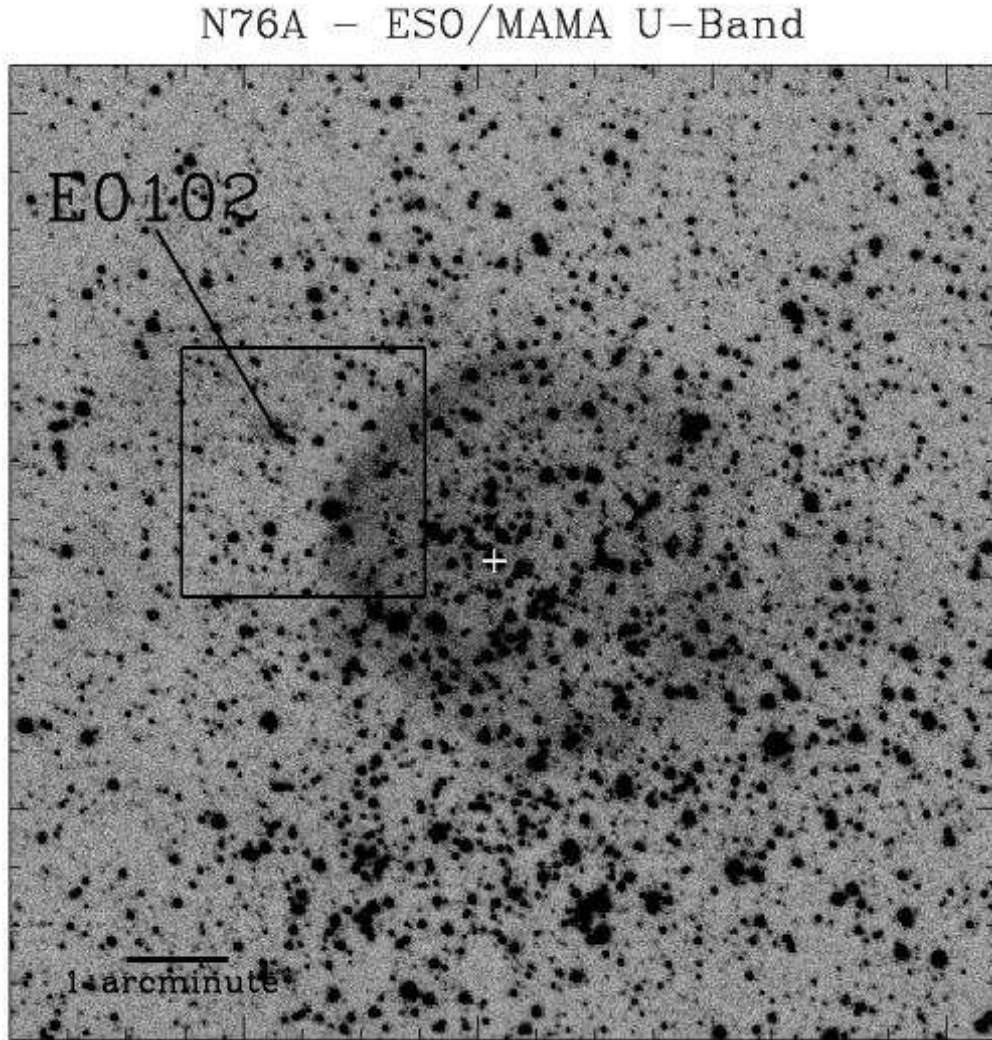


Fig. 1.— An ESO/MAMA *U*-Band image of the N76A nebula and its vicinity. This image includes [OII] $\lambda\lambda 3727$ emission from the N76A nebula and the SNR E0102. The box shows the ACS WFC footprint of the field shown in Figs. 2 and 3, and the white plus sign marks the position of SMC WR7, the WN2 + O6 binary system that ionizes the nebula.

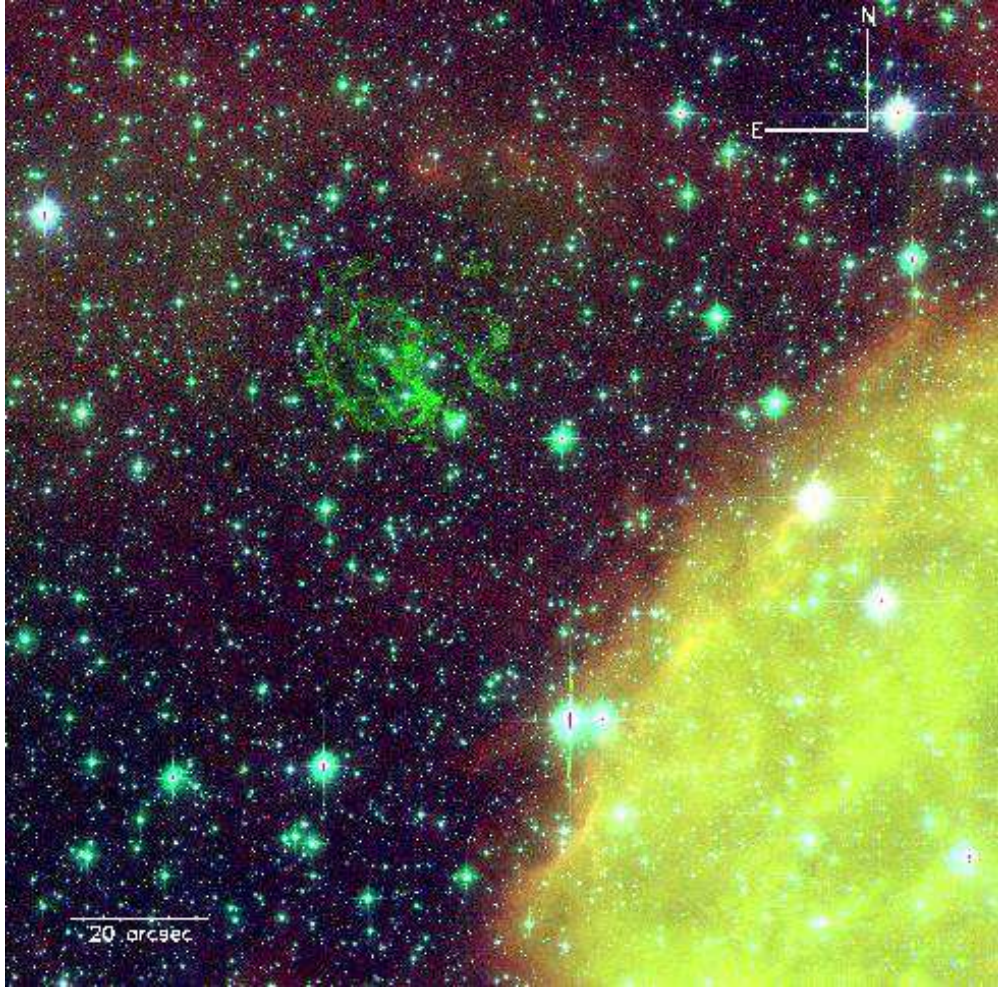


Fig. 2.— A three color ACS WFC image of E0102 and its surroundings, with $H\alpha + [\text{NII}]$ F658N shown in red, $[\text{O III}]$ F475W shown in green, and the continuum F550M shown in blue. E0102 appears green because it is O-rich and lacking in hydrogen. There is a cleared region between E0102 and the surrounding halo that shows the progress of the forward shock; this region is filled with X-rays. The nearby high-excitation N76A nebula is in the lower-right corner.

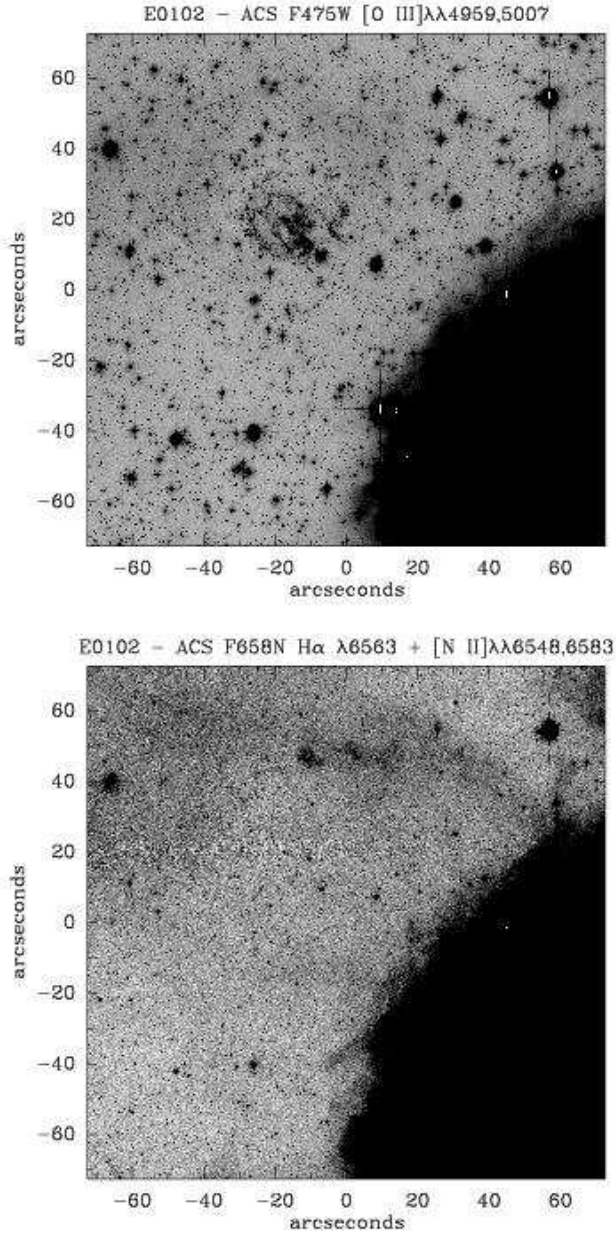


Fig. 3.— (a) [O III] emission from the F475W filter. (b) H α + [NII] emission from the F658N filter. Due to its lack of hydrogen, E0102 is completely absent from the bottom H α + [NII] image. The (0,0) position of these images is at RA 01^h03^m58^s.7, DEC -72°02'14''.8 (J2000).

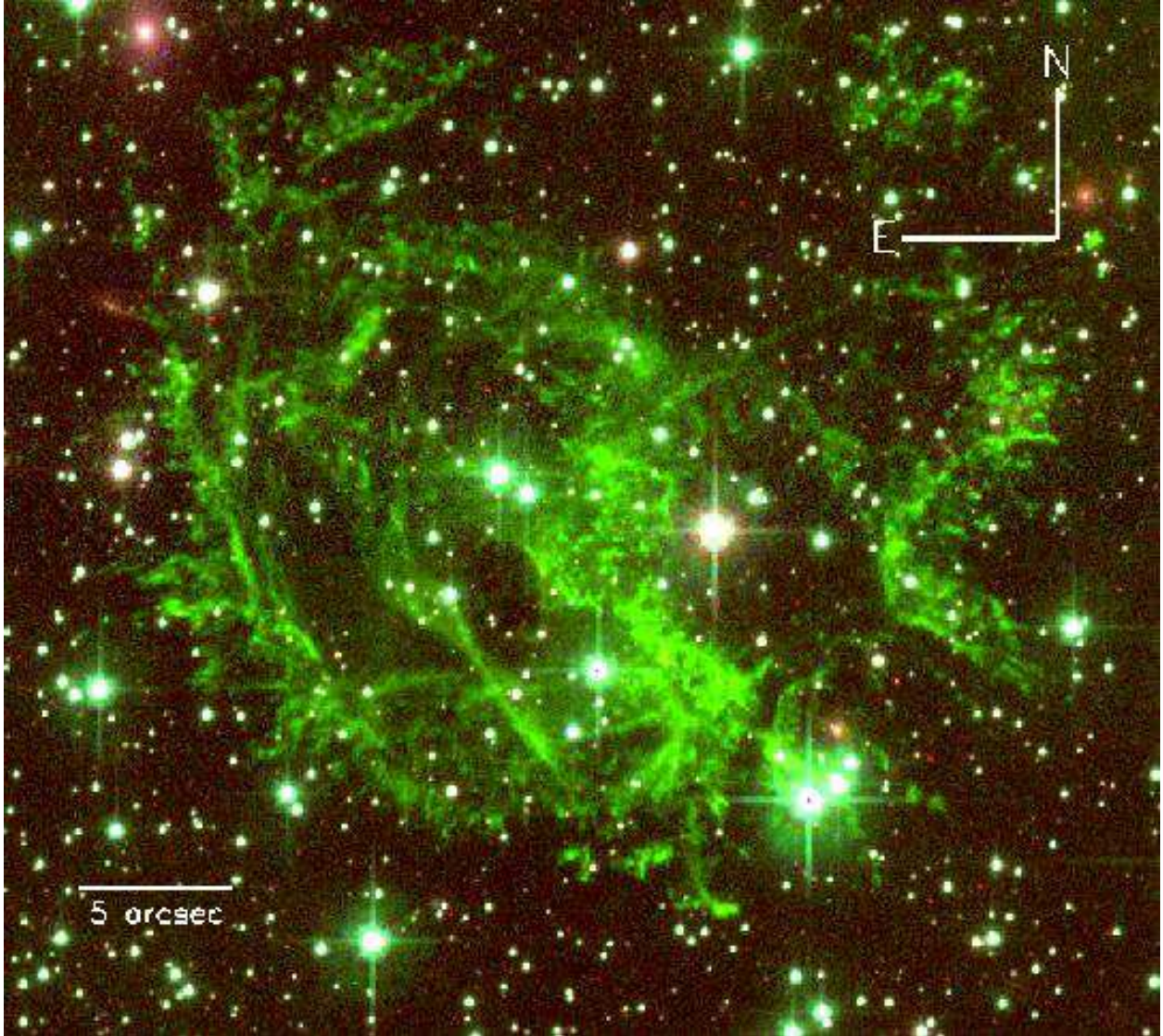


Fig. 4.— A three color ACS WFC close-up image of E0102. Green represents [O III] emission from the F475W filter, blue represents the continuum F550M filter, and red represents the F775W filter. The full velocity structure of the SNR is seen here, showing much of the emission that was Doppler shifted out of the WFPC2 data. The backward S-shaped feature that runs from the northeast to the south-southwest is likely associated with the approaching side of the ejecta shell. The optical distribution is asymmetrical with most of the emission in the southeast quadrant.

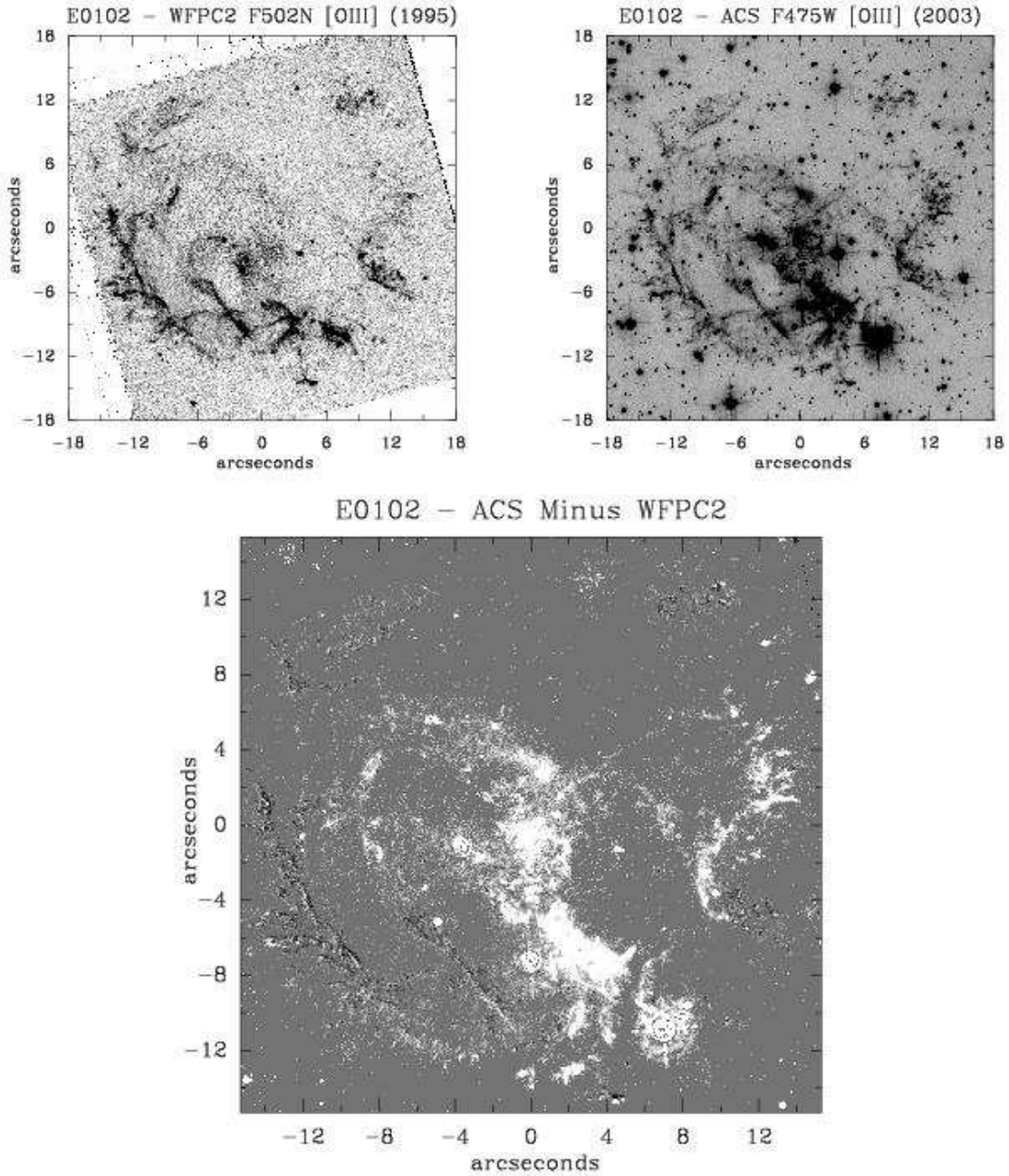


Fig. 5.— (*Top*) WFPC2 1995 epoch and ACS 2003 epoch [O III] images of 1E 0102–7219. These images have been registered using background stars (see Figure 6). The additional emission and increased signal-to-noise are readily apparent in the ACS image. (*Bottom*) A difference image highlighting the motion detected between the two epochs, as well as new emission detected in the 2003 epoch. The ACS 2003 epoch appears white, while the WFPC2 1995 epoch appears black.

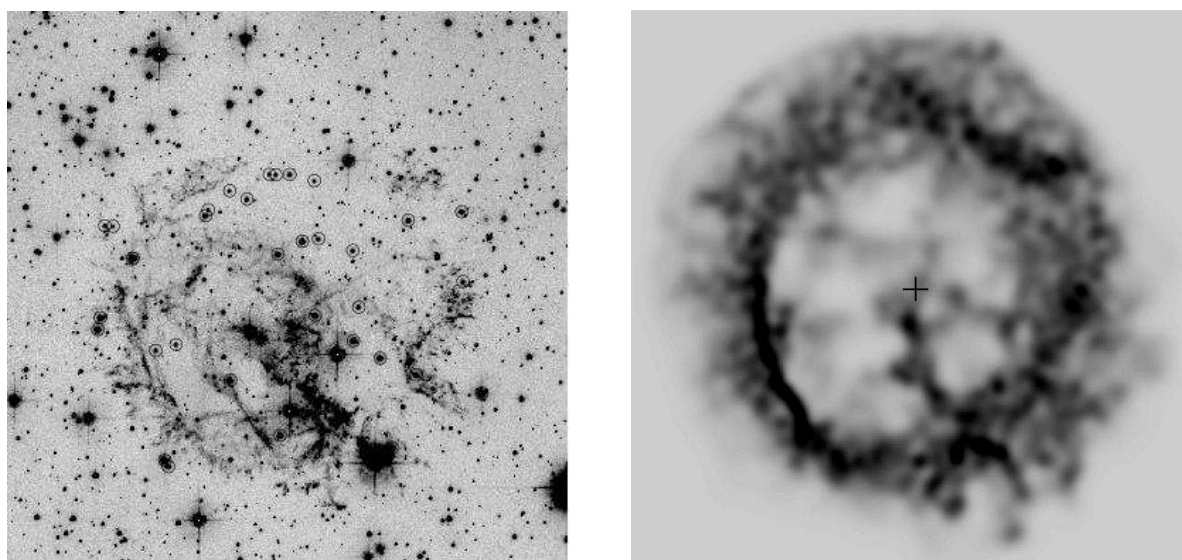


Fig. 6.— (*Left*) ACS [O III] 2003 epoch image of 1E 0102–7219. Circles are drawn around the 40 stars that were used to register this image to the WFPC2 F502N 1995 epoch image (some of the stars are hidden by emission). (*Right*) *Chandra* ACIS-S 1999 X-ray image of E0102. We calculated the geometric center using horizontal and vertical intensity crosscuts. This center is denoted by the plus sign in this image and in Figure 8. The field shown is the same in both figures.

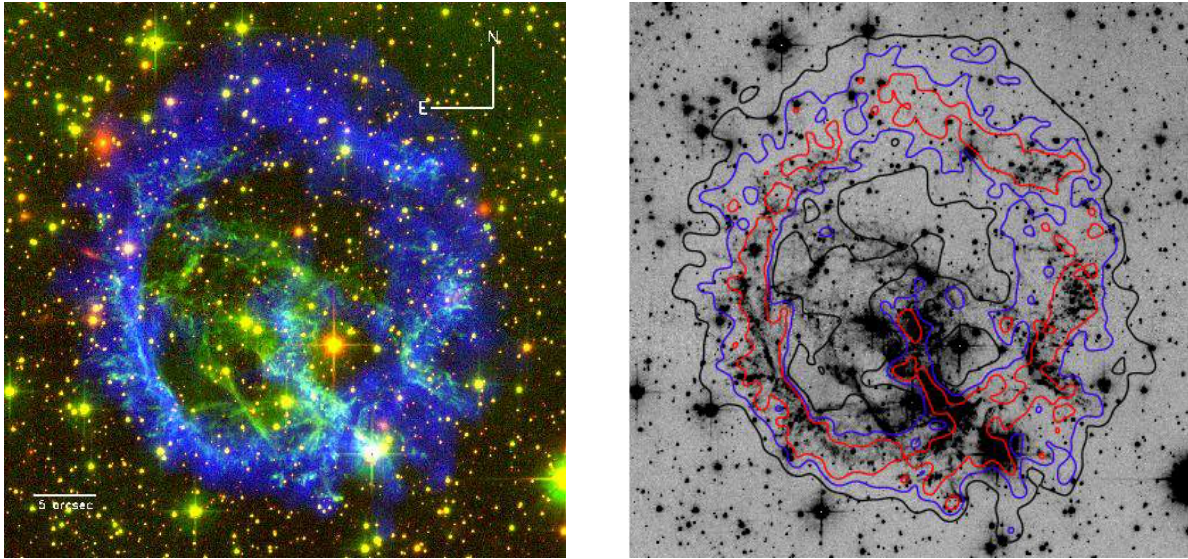


Fig. 7.— (*Left*) Three color image, with the ACS 2003 [O III] in green and the F775W filter in red. The 1999 *Chandra* image is represented in blue. (*Right*) ACS 2003 epoch is shown with contours from the 1999 *Chandra* image overlaid. The red contour marks the brightest X-ray emission and is coincident with the reverse shock, while the black contour outlines the faintest emission with the outer edge at the position of the forward blast wave. The X-ray and optical ejecta emissions correspond in many areas, but are also anti-correlated in several regions.

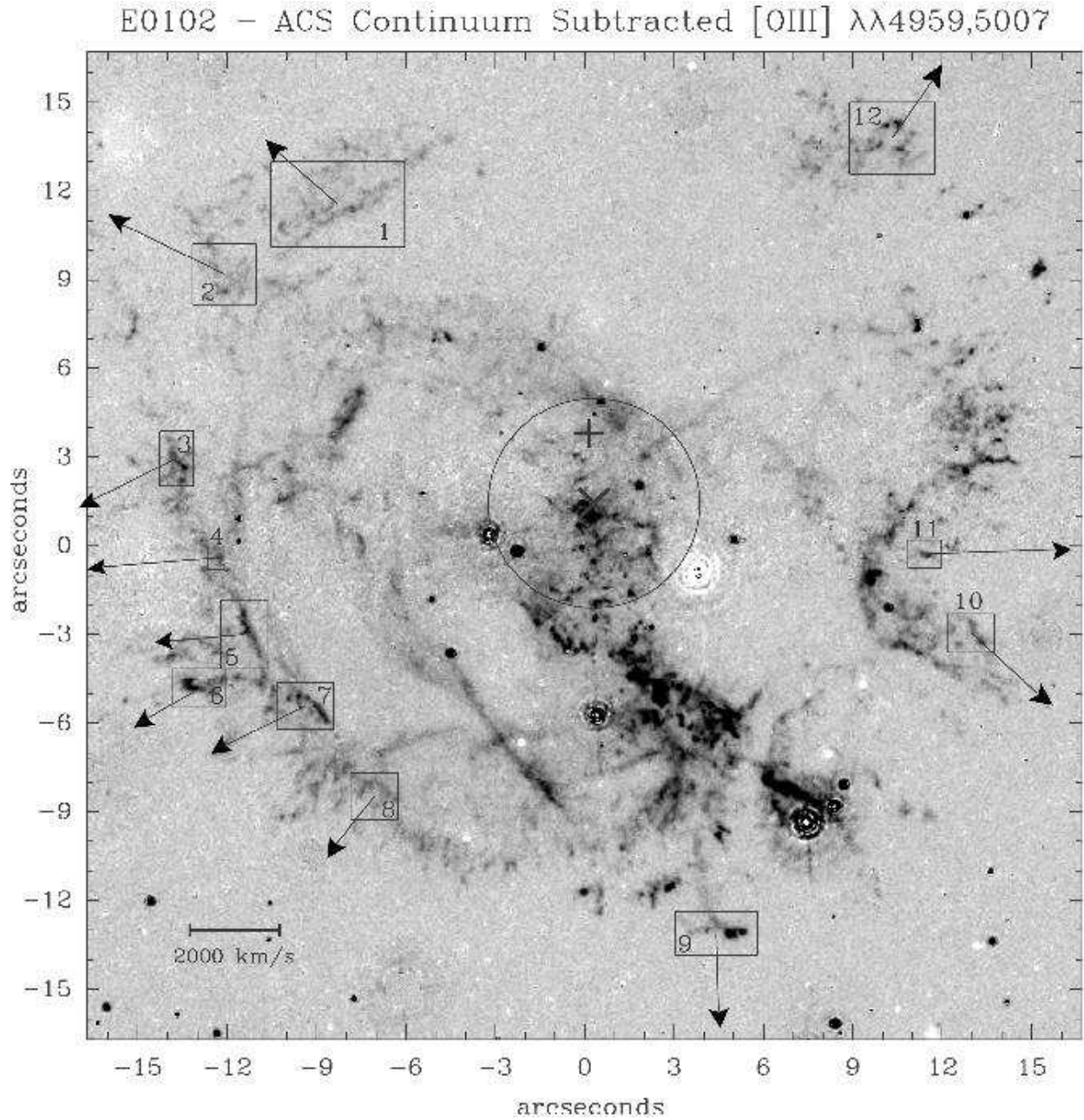


Fig. 8.— The ACS continuum-subtracted [O III] image from 2003 with boxes drawn around the regions that had detectable proper motions. The arrows show the directions of motion of the measured filaments. The line lengths accurately represent the velocity magnitudes, with $1.5'' = 1000 \text{ km s}^{-1}$. The + marks the geometric center, and the \times marks the proper-motion derived center. A 1σ error circle is drawn around the proper-motion derived center (see text for details).